

Toroidal Fermi-surface geometry and phonon-limited transport in nodal-line semimetals

Aman Anand^{1,*} and Alessandro De Martino^{1,†}

¹*Department of Mathematics, City St George's, University of London, London EC1V 0HB, United Kingdom*

Nodal-line semimetals (NLSs) can display unconventional quasiparticle dynamics and charge transport properties due to their extended band degeneracy and the peculiar geometry of their Fermi surface. We consider electronacoustic phonon scattering as the dominant relaxation mechanism and compute the quasiparticle decay rate and dc conductivity by solving the linearized semiclassical Boltzmann equation in a minimal model of a doped circular NLS. We find that the toroidal geometry of the Fermi surface gives rise to two parametrically distinct Bloch–Grüneisen temperatures, associated with momentum transfers along the poloidal and toroidal directions, respectively. As a result, an intermediate temperature window opens between these two scales, in which the decay rate follows $\Gamma \propto T^2$, while the conductivity follows $\sigma \propto T^{-2}$. We also obtain the low- and high-temperature asymptotic behaviors, and discuss implications for ARPES and transport measurements in candidate NLS materials.

I. INTRODUCTION

Topological semimetals have emerged in recent years as a new platform for studying materials with symmetry- and topology-protected band crossings and the unconventional transport properties that can result [1–5]. Among them, nodal-line semimetals (NLSs) [6–10], in which valence and conduction bands touch along one-dimensional manifolds in momentum space, provide a particularly rich setting. Prototypical NLSs such as ZrSiS [11–13] host Dirac-like nodal lines and exhibit unusual phenomena, including large magnetoresistance [14–17], high carrier mobilities [17, 18], pronounced Zeeman splitting [19], and enhanced quasiparticle masses near the nodal lines [20], revealed by quantum oscillation experiments. Transport in these systems has been explored in various regimes, showing unique signatures both in the quantum diffusive regime and in the presence of magnetic fields [21–31].

Impurity-limited transport has been analyzed in Ref. [22], where the conductivity was studied as a function of temperature, chemical potential, and impurity concentration. They noted that impurity potentials are strongly screened at elevated chemical potential. Experimentally, exceptionally clean samples of NLSs have been realized, like ZrSiS crystals displaying a large residual resistivity ratio, $\rho(300\text{ K})/\rho(2\text{ K}) = 288$ [16]. These observations suggest the existence of a parameter window in temperature and chemical potential in which charge transport may be limited by inelastic scattering rather than disorder.

In this regime, electronphonon interactions [32–35] are expected to play a central role. In Ref. [32], these interactions were investigated with particular focus on optical phonons. The phonon spectrum of ZrSiS presented therein revealed that below 10 meV ($\approx 116\text{ K}$), only acous-

tic phonons are available for scattering. Signatures of electronphonon scattering are observable in transport measurements as well as in angle-resolved photoemission spectroscopy (ARPES). ARPES studies [36, 37] on materials such as PbTaSe₂ and the ZrSiX ($X = \text{S, Se, Te}$) family have revealed nodal-line dispersions and provided insights into quasiparticle lifetimes.

In conventional metals with large Fermi surfaces, the electronphonon scattering rate exhibits two characteristic temperature regimes set by the Debye temperature [38, 39]. In semimetals, owing to the small size of the Fermi surface, the analogous crossover is controlled by a Bloch–Grüneisen (BG) temperature, set by the maximal phonon momentum allowed for scattering on the Fermi surface [40]. For Weyl semimetals, electron–acoustic phonon scattering (both in bulk and in Fermi-arc states) and the role of the BG scales have been discussed in Refs. [41, 42], while related BlochGrüneisen physics has been explored experimentally in Dirac semimetals [43]. However, a systematic analysis analogous to this for NLSs, where the Fermi surface acquires a toroidal geometry, is still lacking.

This motivates our study of electron-acoustic phonon scattering in NLSs in the clean limit. We focus on temperatures below the scale set by optical phonons and well below the chemical potential, so that interband processes are negligible. Notably, in non-symmorphic NLSs, the chemical potential can be tuned not only by doping but also via anisotropic strain [44], providing experimental access to the regime we consider. While here we study how phonons affect electronic lifetime and transport, we note that the reciprocal problem of electron-induced renormalization of phonon properties has been addressed in Refs. [34, 45–47].

We solve the linearized Boltzmann transport equation (BTE) exactly in the thin-torus limit by exploiting the fact that the leading-order scattering kernel depends only on angular differences on the torus. Our main finding is that the toroidal geometry gives rise to two parametrically different BG temperatures, related to the two distinct radii of the Fermi surface. The coexistence of

* Aman.Anand@citystgeorges.ac.uk

† Alessandro.De-Martino.1@citystgeorges.ac.uk

these two independent scales leads to a qualitatively new intermediate regime in which the phase space for electron-phonon scattering is modified, yielding a quasiparticle decay rate $\Gamma \propto T^2$ and a conductivity $\sigma \propto T^{-2}$. In addition, we find the usual behaviours $\Gamma \propto T^3$ and $\sigma \propto T^{-5}$ at low temperatures and $\Gamma \propto T$ with conductivity $\sigma \propto T^{-1}$ at high temperatures. A summary of these scaling regimes is provided in Table I. The intermediate T^2 dependence has a transparent physical origin: in this temperature window, phonon momenta exceed the minor Fermi-surface radius but remain smaller than the major radius, so the scattering phase space along the poloidal direction has saturated while the toroidal direction is still thermally restricted, resulting in a partial saturation that is unique to the toroidal geometry. Since a T^2 resistivity is frequently taken as a hallmark of electron-electron scattering [39, 48], our results show that, in the circular NLS model considered here, the same scaling can also arise from intraband electron-phonon scattering, without invoking electron-electron interactions. We further observe an enhancement of the conductivity anisotropy at elevated temperatures.

The remainder of the paper is structured as follows. In Sec. II, we introduce the electronic and phonon models, the deformation-potential coupling, and the BG temperature scales. In Sec. III we briefly review the formulation of the linearized BTE and derive integral expressions for the decay rate and the transport lifetime. Sections IV and V present the asymptotic temperature dependences, together with numerical evaluations that confirm the predicted power laws. Finally, in Sec. VI we conclude with a discussion of experimental implications and possible extensions. Technical details are collected in several Appendices.

II. MODEL

In this section, we introduce the ingredients entering our transport calculation: a minimal two-band model for a circular NLS, acoustic phonons within an elastic continuum description, and their coupling via the deformation potential. We focus on the highly doped, low-temperature regime with chemical potential $\mu \gg k_B T$, where transport is dominated by intraband scattering processes in the conduction band. Throughout, we set $\hbar = 1$. We consider systems in which the nodal line is approximately flat in energy, as realized, e.g., in Ca_3P_2 [8] and strained YN [49]. Energy dispersion along the nodal contour would introduce an additional competing scale; its effect is discussed in Sec. VI. The toroidal Fermi surface that emerges at finite doping naturally introduces two distinct BG scales, discussed in Sec. IID, which set the relevant temperature regimes for scattering and transport discussed in Secs. IV and V.

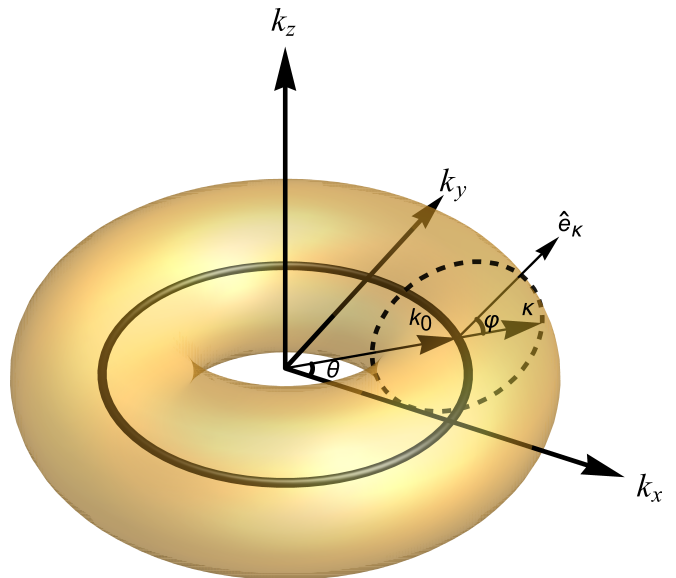


Figure 1. Shown are the toroidal Fermi surface, the associated toroidal coordinates $(\kappa, \theta, \varphi)$, and the unit vector \hat{e}_κ , defined in Eq. (13).

A. Electronic model

We model low-energy quasiparticles in the vicinity of a circular nodal ring (NR) by the two-band effective Hamiltonian [6, 8, 21]

$$\mathcal{H}(\mathbf{k}) = vk_z\sigma_y + \lambda(k^2 - k_0^2)\sigma_z, \quad (1)$$

where $k = \sqrt{k_x^2 + k_y^2 + k_z^2}$, σ_i are Pauli matrices, and v, λ, k_0 are material-dependent parameters. The nodal ring lies in the plane $k_z = 0$ at radius k_0 . It is convenient to define $v_0 = 2\lambda k_0$ and $\alpha = v/v_0$, where v_0 sets the characteristic in-plane velocity near the NR and α parametrizes the anisotropy along k_z [21]. Representative values from DFT for Ca_3P_2 are $v \simeq 2.5 \text{ eV}\text{\AA}$, $\lambda \simeq 4.34 \text{ eV}\text{\AA}^2$, and $k_0 = 0.206 \text{ \AA}^{-1}$ [8], corresponding to $\alpha \simeq 1.4$ and $v_0 \simeq 2.6 \times 10^5 \text{ m/s}$. A small anisotropy may affect numerical prefactors and weakly rescale the BG temperatures, but we do not expect it to significantly affect the temperature exponents, therefore we set $\alpha = 1$ hereafter.

The electronic eigenstates are

$$|\Phi_{\mathbf{k},\zeta}(\mathbf{r})\rangle = e^{i\mathbf{k}\cdot\mathbf{r}}|u_{\mathbf{k},\zeta}\rangle, \quad (2)$$

where $|u_{\mathbf{k},\zeta}\rangle$ diagonalize $\mathcal{H}(\mathbf{k})$ with eigenvalues

$$\varepsilon_{\mathbf{k},\zeta} = \zeta \sqrt{v^2 k_z^2 + \lambda^2 (k^2 - k_0^2)^2}, \quad (3)$$

and $\zeta = \pm$ labels conduction/valence bands. The corresponding Bloch spinors can be written as

$$|u_{\mathbf{k},\zeta}\rangle = \mathcal{N}_{\mathbf{k},\zeta} \begin{pmatrix} ivk_z \\ \lambda(k^2 - k_0^2) - \varepsilon_{\mathbf{k},\zeta} \end{pmatrix}, \quad (4)$$

with normalization fixed by $\langle u_{\mathbf{k},\zeta'} | u_{\mathbf{k},\zeta} \rangle = \delta_{\zeta,\zeta'}$. The group velocity $\mathbf{v}_\zeta(\mathbf{k}) = \partial_{\mathbf{k}} \varepsilon_{\mathbf{k},\zeta}$ is given by

$$\mathbf{v}_\zeta(\mathbf{k}) = \frac{2\lambda^2(\mathbf{k}^2 - k_0^2)}{\varepsilon_{\mathbf{k},\zeta}} \mathbf{k} + \frac{v^2}{\varepsilon_{\mathbf{k},\zeta}} k_z \hat{z}. \quad (5)$$

For energies well below the Lifshitz scale $\varepsilon_{\mathbf{k},\zeta} \ll \lambda k_0^2$, constant-energy surfaces form a thin torus in momentum space (see Fig. 1). It is then convenient to introduce toroidal coordinates $(\kappa, \theta, \varphi)$

$$k_x = (k_0 + \kappa \cos \varphi) \cos \theta, \quad (6)$$

$$k_y = (k_0 + \kappa \cos \varphi) \sin \theta, \quad (7)$$

$$k_z = \kappa \sin \varphi, \quad (8)$$

where κ is the minor radius, $\theta \in [0, 2\pi)$ the toroidal angle (along the NR), and $\varphi \in [0, 2\pi)$ the poloidal angle (around the tube cross-section). In the thin-torus regime $\kappa \ll k_0$, one may expand $k^2 - k_0^2 \simeq 2k_0\kappa \cos \varphi$ and obtain the Dirac-like form

$$\mathcal{H}(\kappa, \theta, \varphi) = v_0 \kappa (\cos \varphi \sigma_z + \sin \varphi \sigma_y), \quad (9)$$

with dispersion

$$\varepsilon_{\mathbf{k},\zeta} = \zeta v_0 \kappa. \quad (10)$$

Such linear behaviour has been observed over a broad energy window in several NLS materials, including ZrSiS [11, 12].

In these coordinates, the spinors simplify to

$$|u_{\mathbf{k},+}\rangle = \begin{pmatrix} \cos \varphi/2 \\ i \sin \varphi/2 \end{pmatrix}, \quad |u_{\mathbf{k},-}\rangle = \begin{pmatrix} -\sin \varphi/2 \\ i \cos \varphi/2 \end{pmatrix}. \quad (11)$$

and the conduction-band group velocity becomes

$$\mathbf{v}_+(\mathbf{k}) = v_0 \hat{e}_\kappa, \quad (12)$$

where the unit vector \hat{e}_κ (shown in Fig. 1) reads

$$\hat{e}_\kappa = \cos \varphi \cos \theta \hat{x} + \cos \varphi \sin \theta \hat{y} + \sin \varphi \hat{z}. \quad (13)$$

Since we focus here on temperatures $k_B T \ll \mu$, the valence band does not contribute, and we restrict attention to $\zeta = +$, suppressing the band index hereafter.

B. Phonon model

We describe acoustic lattice vibrations within isotropic elastic continuum theory [50]. In this approximation, the phonon spectrum is determined by the longitudinal and transverse sound velocities c_l and c_t . These velocities are typically much smaller than the electronic Fermi velocity; for example, in ZrSiS one finds $c_l \simeq 3.2 \times 10^3$ m/s [32] and $v_0 \simeq 6.5 \times 10^5$ m/s [11], so that $c_l/v_0 \sim 10^{-2}$.

The displacement field $\mathbf{u}(\mathbf{r}, t)$ obeys the wave equation

$$\nabla_t^2 \mathbf{u} = c_t^2 \nabla^2 \mathbf{u} + (c_l^2 - c_t^2) \nabla(\nabla \cdot \mathbf{u}), \quad (14)$$

which, for harmonic time dependence $\mathbf{u}(\mathbf{r}, t) = \mathbf{u}(\mathbf{r}) e^{-i\Omega t}$, becomes

$$-\Omega^2 \mathbf{u} = c_t^2 \nabla^2 \mathbf{u} + (c_l^2 - c_t^2) \nabla(\nabla \cdot \mathbf{u}). \quad (15)$$

Its normal modes are one longitudinal and two transverse acoustic branches with dispersions $\Omega_{\mathbf{q}}^{(l/t)} = c_{l/t} |\mathbf{q}|$.

In the deformation-potential approximation, which we introduce in Sec. II C, only longitudinal lattice deformations contribute. So in what follows, we restrict ourselves to the longitudinal mode and we suppress the branch label in phonon operators and frequencies henceforth. Upon quantization, the longitudinal displacement field can be expanded as

$$\mathbf{u}(\mathbf{r}) = \int d^3 \mathbf{q} \frac{e^{i\mathbf{q}\cdot\mathbf{r}}}{\sqrt{2\rho_M \Omega_{\mathbf{q}}}} \hat{\mathbf{q}} \left[a_{\mathbf{q}} - a_{-\mathbf{q}}^\dagger \right], \quad (16)$$

where ρ_M is the mass density of the medium, $a_{\mathbf{q}}^\dagger$, $a_{\mathbf{q}}$ are longitudinal phonon creation and annihilation operators, and $\hat{\mathbf{q}} = \mathbf{q}/|\mathbf{q}|$.

C. Electron-phonon interaction

We consider electronphonon interactions via the deformation potential,

$$H_{\text{ep}} = g_0 \nabla \cdot \mathbf{u}(\mathbf{r}), \quad (17)$$

where the coupling constant g_0 parametrizes the shift of the electronic band energy under local compression and is taken diagonal in spin-orbital space. In principle, this coupling is renormalized by electronic screening, which we do not explicitly consider here. We therefore treat g_0 as an effective (screened) deformation-potential coupling, which may have a weak μ dependence.

Since $\nabla \cdot \mathbf{u} = 0$ for transverse modes, only longitudinal phonons contribute to the electron-phonon coupling. Other coupling mechanisms have also been explored, for example strain-induced effective gauge fields leading to a topological piezoelectric response in NLSs [51]. We neglect piezoelectric effects here because several NLSs of interest, including Ca_3P_2 and ZrSiS, are centrosymmetric and cannot exhibit conventional bulk piezoelectricity [8, 11, 52]. In these systems, the deformation potential is expected to provide the dominant coupling between electron and acoustic phonons.

Substituting the mode expansion (16), into H_{ep} and evaluating matrix elements between Bloch states $|\Phi_{\mathbf{k}}\rangle$ and $|\Phi_{\mathbf{k}'}\rangle$ yields

$$\langle \Phi_{\mathbf{k}'} | H_{\text{ep}} | \Phi_{\mathbf{k}} \rangle = \mathcal{G}_{\mathbf{k},\mathbf{k}'} \left(a_{\mathbf{q}} - a_{-\mathbf{q}}^\dagger \right), \quad (18)$$

with momentum transfer $\mathbf{q} = \mathbf{k}' - \mathbf{k}$ and amplitude

$$\mathcal{G}_{\mathbf{k},\mathbf{k}'} = i \frac{g_0 \sqrt{\Omega_{\mathbf{q}}}}{c_l \sqrt{2\rho_M}} \langle u_{\mathbf{k}'} | u_{\mathbf{k}} \rangle. \quad (19)$$

The pseudospin dependence enters through the Bloch spinor overlap $\langle u_{\mathbf{k}'} | u_{\mathbf{k}} \rangle$, which in toroidal coordinates follows from Eq. (11) (for the conduction band) as

$$\langle u_{\mathbf{k}'} | u_{\mathbf{k}} \rangle = \cos\left(\frac{\varphi - \varphi'}{2}\right). \quad (20)$$

Assuming that phonons are in thermal equilibrium at temperature T , the transition rate from the electronic state $|\Phi_{\mathbf{k}}\rangle$ to $|\Phi_{\mathbf{k}'}\rangle$ follows from Fermi's golden rule as

$$W_{\mathbf{k}',\mathbf{k}} = 2\pi |\mathcal{G}_{\mathbf{k}',\mathbf{k}}|^2 \left\{ n_B(\Omega_{\mathbf{q}}) \delta(\varepsilon_{\mathbf{k}'} - \varepsilon_{\mathbf{k}} - \Omega_{\mathbf{q}}) + [n_B(\Omega_{\mathbf{q}}) + 1] \delta(\varepsilon_{\mathbf{k}'} - \varepsilon_{\mathbf{k}} + \Omega_{\mathbf{q}}) \right\}, \quad (21)$$

where $n_B(\Omega) = 1/(e^{\beta\Omega} - 1)$ is the Bose-Einstein distribution function, with $\beta = 1/k_B T$. The two terms in Eq. (21) describe phonon absorption and emission, respectively. These rates enter the collision integral of the Boltzmann equation in Sec. III.

D. Temperature scales

In conventional metals with large Fermi surfaces, the crossover between low- and high-temperature regimes of electron-phonon scattering is usually controlled by the Debye temperature. In semimetals, instead, the crossover is controlled by the BG temperature, set by the maximal phonon momentum that can scatter carriers across the Fermi surface. For a toroidal Fermi surface, there are two independent momentum scales, corresponding to the minor and major radii, and thus two BG scales. We define

$$k_B T_{\text{BG}}^{(\text{pol})} = 2c_l \kappa_F, \quad (22)$$

$$k_B T_{\text{BG}}^{(\text{tor})} = c_l k_0, \quad (23)$$

where k_B is the Boltzmann constant and $\kappa_F = \mu/v_0$ is the minor radius of the toroidal Fermi surface at chemical potential μ . The scale $T_{\text{BG}}^{(\text{pol})}$ is associated with momentum transfer along the poloidal direction, set by κ_F , while $T_{\text{BG}}^{(\text{tor})}$ reflects the toroidal extent along the NR, set by k_0 .

For illustration, in PbTaSe₂, a NLS with strong spin-orbit coupling [36], one has $k_0 \simeq 0.2 \text{ \AA}^{-1}$ and $c_l \simeq 3.2 \times 10^3 \text{ m/s}$ [53], yielding

$$T_{\text{BG}}^{(\text{tor})} = \frac{c_l k_0}{k_B} \simeq 49 \text{ K}. \quad (24)$$

For ZrSiS, the nodal line is approximately diamond-shaped, but taking $k_0 \simeq 0.3 \text{ \AA}^{-1}$ [54] and $c_l \simeq 6.8 \times 10^3 \text{ m/s}$ [32] gives

$$T_{\text{BG}}^{(\text{tor})} = \frac{c_l k_0}{k_B} \simeq 156 \text{ K}. \quad (25)$$

The Debye temperatures in these materials are typically several times larger than $T_{\text{BG}}^{(\text{tor})}$ [17, 55], justifying the use of long-wavelength acoustic phonons with linear dispersion in the temperature ranges of interest.

In our model, we assume a thin torus, $\kappa_F \ll k_0$, which implies the hierarchy

$$T_{\text{BG}}^{(\text{pol})}/T_{\text{BG}}^{(\text{tor})} \sim \kappa_F/k_0 \ll 1. \quad (26)$$

This naturally leads to three temperature regimes that will control both quasiparticle decay rate and transport scattering rate: (i) $T \ll T_{\text{BG}}^{(\text{pol})}$, (ii) $T_{\text{BG}}^{(\text{pol})} \ll T \ll T_{\text{BG}}^{(\text{tor})}$, and (iii) $T \gg T_{\text{BG}}^{(\text{tor})}$.

In the next section, we formulate the semiclassical BTE using the transition rates in Eq. (21) and derive expressions for the decay rate and transport lifetime in these regimes.

III. BOLTZMANN EQUATION

In this section, we briefly review the formulation of semiclassical charge transport in the presence of electron-phonon scattering within the BTE framework [38]. We then solve the linearized BTE in terms of transport lifetimes τ_{tr}^i ($i = x, y, z$), which we use to evaluate the conductivity tensor in Sec. V. The same scattering kernel, without the transport weighting factor, also gives the single-particle decay rate Γ , discussed in Sec. IV.

A. Linearized BTE

In the presence of slowly varying external fields, the semiclassical BTE for the electron distribution function $f(\mathbf{r}, \mathbf{k}, t)$ reads [56]

$$\frac{\partial f}{\partial t} + \mathbf{v}(\mathbf{k}) \cdot \nabla_{\mathbf{r}} f + \mathbf{F}_{\text{ext}} \cdot \nabla_{\mathbf{k}} f = \mathcal{I}_{\mathbf{k}}, \quad (27)$$

where $\mathcal{I}_{\mathbf{k}}$ is the collision integral, $\mathbf{v}(\mathbf{k})$ is the electron group velocity and $\mathbf{F}_{\text{ext}} = e\mathbf{E}$ for a uniform electric field with e the electron charge. For a homogeneous steady state ($\partial_t f = \nabla_{\mathbf{r}} f = 0$), driven by a weak uniform electric field \mathbf{E} , Eq. (27) becomes

$$e\mathbf{E} \cdot \nabla_{\mathbf{k}} f_{\mathbf{k}} = \mathcal{I}_{\mathbf{k}}. \quad (28)$$

The collision integral for scattering between states \mathbf{k} and \mathbf{k}' mediated by phonons can be written as

$$\mathcal{I}_{\mathbf{k}} = \int \frac{d^3 \mathbf{k}'}{(2\pi)^3} \{ W_{\mathbf{k},\mathbf{k}'} f_{\mathbf{k}'} (1 - f_{\mathbf{k}}) - W_{\mathbf{k}',\mathbf{k}} f_{\mathbf{k}} (1 - f_{\mathbf{k}'} \} \}, \quad (29)$$

where $W_{\mathbf{k}',\mathbf{k}}$ is the transition rate from \mathbf{k} to \mathbf{k}' obtained from Fermi's golden rule [cf. Eq. (21)].

We now linearize the BTE around equilibrium by writing

$$f_{\mathbf{k}} = n_F(\varepsilon_{\mathbf{k}}) - \varphi_{\mathbf{k}} \frac{\partial n_F(\varepsilon_{\mathbf{k}})}{\partial \varepsilon_{\mathbf{k}}}, \quad (30)$$

where $n_F(\varepsilon) = 1/(e^{\beta(\varepsilon-\mu)} + 1)$ is the Fermi-Dirac distribution function at chemical potential μ , and $\varphi_{\mathbf{k}}$ is a function parametrizing the deviation from equilibrium. Standard manipulations using detailed balance (summarized in Appendix A) recast the linearized collision inte-

gral as

$$\mathcal{I}_{\mathbf{k}} = \frac{\partial n_F(\varepsilon_{\mathbf{k}})}{\partial \varepsilon_{\mathbf{k}}} \mathcal{J}_{\mathbf{k}}, \quad \mathcal{J}_{\mathbf{k}} \equiv \int \frac{d^3 \mathbf{k}'}{(2\pi)^3} \mathcal{W}_{\mathbf{k}',\mathbf{k}}(\varphi_{\mathbf{k}} - \varphi_{\mathbf{k}'}), \quad (31)$$

where the symmetric kernel $\mathcal{W}_{\mathbf{k}',\mathbf{k}}$ is given by

$$\mathcal{W}_{\mathbf{k}',\mathbf{k}} = 2\pi |\mathcal{G}_{\mathbf{k}',\mathbf{k}}|^2 \{ [n_B(\Omega_{\mathbf{q}}) + n_F(\varepsilon_{\mathbf{k}} + \Omega_{\mathbf{q}})] \delta(\varepsilon_{\mathbf{k}'} - \varepsilon_{\mathbf{k}} - \Omega_{\mathbf{q}}) + [n_B(\Omega_{\mathbf{q}}) + 1 - n_F(\varepsilon_{\mathbf{k}} - \Omega_{\mathbf{q}})] \delta(\varepsilon_{\mathbf{k}'} - \varepsilon_{\mathbf{k}} + \Omega_{\mathbf{q}}) \}, \quad (32)$$

with $\mathbf{q} = \mathbf{k}' - \mathbf{k}$, and $\Omega_{\mathbf{q}} = c_l |\mathbf{q}|$. Inserting Eq. (31) into Eq. (28) yields the linearized BTE

$$e\mathbf{E} \cdot \mathbf{v}(\mathbf{k}) = \mathcal{J}_{\mathbf{k}}. \quad (33)$$

In the rest of this paper, we specialize to the degenerate, thin-torus regime. Specifically, we assume $k_B T \ll \mu$ so that transport is controlled by quasiparticles at the Fermi surface, and we set $-\partial_{\varepsilon} n_F(\varepsilon) \simeq \delta(\varepsilon - \mu)$. Moreover, since $c_l \ll v_0$, typical phonon energies are small compared with electronic scales, so scattering is quasi-elastic ($\Omega_{\mathbf{q}} \ll \mu$ for thermal phonons), and we therefore omit the phonon energy in the energy-conserving δ -functions in the scattering rates (32). The combinations of Fermi and Bose functions evaluated at $\varepsilon_{\mathbf{k}} = \mu$, simplify to

$$\begin{aligned} n_B(\Omega_{\mathbf{q}}) + n_F(\varepsilon_{\mathbf{k}} + \Omega_{\mathbf{q}}) &= \frac{1}{\sinh(\beta\Omega_{\mathbf{q}})} \\ &= n_B(\Omega_{\mathbf{q}}) + 1 - n_F(\varepsilon_{\mathbf{k}} - \Omega_{\mathbf{q}}), \end{aligned} \quad (34)$$

so that the kernel in Eq. (32) takes the form

$$\mathcal{W}_{\mathbf{k}',\mathbf{k}} = \widetilde{\mathcal{W}}_{\mathbf{k}',\mathbf{k}} \delta(\varepsilon_{\mathbf{k}'} - \varepsilon_{\mathbf{k}}), \quad (35)$$

with

$$\widetilde{\mathcal{W}}_{\mathbf{k}',\mathbf{k}} = \frac{4\pi |\mathcal{G}_{\mathbf{k}',\mathbf{k}}|^2}{\sinh(\beta c_l |\mathbf{q}|)}. \quad (36)$$

Finally, the phase space integral reduces to an integration over the toroidal Fermi surface which, in the thin-torus limit $\kappa_F/k_0 \ll 1$, reads

$$\int \frac{d^3 \mathbf{k}'}{(2\pi)^3} \delta(\varepsilon_{\mathbf{k}'} - \mu) \dots \approx \frac{\kappa_F k_0}{(2\pi)^3 v_0} \int d\varphi' d\theta' \dots, \quad (37)$$

where we have used the Jacobian of the transformation to toroidal coordinates $\kappa'(k_0 + \kappa' \cos \varphi')$, evaluated on the Fermi surface $\kappa' = \kappa_F$, and the linear dispersion in Eq. (10); at leading order in κ_F/k_0 , we set $k_0 + \kappa_F \cos \varphi' \approx k_0$. In this limit, the momentum transfer between states \mathbf{k} and \mathbf{k}' simplifies to (see Appendix C for details)

$$|\mathbf{q}| = |\mathbf{k} - \mathbf{k}'| = \sqrt{4k_0^2 \sin^2\left(\frac{\theta - \theta'}{2}\right) + 4\kappa_F^2 \sin^2\left(\frac{\varphi - \varphi'}{2}\right)}. \quad (38)$$

Moreover, using Eq. (20), the Bloch spinor overlap $\langle u_{\mathbf{k}'} | u_{\mathbf{k}} \rangle$ depends only on the poloidal angle difference $\varphi - \varphi'$. Therefore the scattering kernel $\widetilde{\mathcal{W}}_{\mathbf{k}',\mathbf{k}}$ depends on initial and final momenta only through toroidal and poloidal angle differences and is translationally invariant on the toroidal Fermi surface to leading order in κ_F/k_0 .

Under the approximations discussed above, the linearized BTE can be solved exactly to leading order in κ_F/k_0 , as discussed next.

B. Transport lifetimes

To solve Eq. (33) we make the ansatz

$$\varphi_{\mathbf{k}} = e\mathbf{E} \cdot \mathbf{\Lambda}_{\mathbf{k}}, \quad (39)$$

where $\mathbf{\Lambda}_{\mathbf{k}}$ is the vector mean free path [38]. Upon inserting Eq. (39) into Eq. (33) and using Eqs. (12), (37), and the fact that the direction of \mathbf{E} is arbitrary, we arrive at the integral equation on the Fermi torus

$$\hat{e}_{\kappa} = \frac{\kappa_F k_0}{(2\pi)^3 v_0^2} \int d\varphi' d\theta' \widetilde{\mathcal{W}}_{\mathbf{k}',\mathbf{k}}(\mathbf{\Lambda}_{\mathbf{k}} - \mathbf{\Lambda}_{\mathbf{k}'}). \quad (40)$$

Since to leading order in κ_F/k_0 , the kernel $\widetilde{\mathcal{W}}_{\mathbf{k}',\mathbf{k}}$ depends only on angle differences, $\widetilde{\mathcal{W}}_{\mathbf{k}',\mathbf{k}} = \widetilde{\mathcal{W}}(\theta - \theta', \varphi - \varphi')$, the collision integral is a convolution on the torus, so the collision operator is diagonal in the double Fourier basis $e^{im\theta + in\varphi}$. We show in Appendix B that the exact solution of Eq. (40) reads

$$\Lambda_{\mathbf{k}}^i = v_0 \tau_{\text{tr}}^i e_{\kappa}^i, \quad i = x, y, z, \quad (41)$$

where the scattering lifetimes, evaluated at the chemical potential μ , are given by

$$\Gamma_{\text{tr}}^{x,y} = \frac{1}{\tau_{\text{tr}}^{x,y}} = \frac{\kappa_F k_0}{(2\pi)^3 v_0} \int d\varphi' d\theta' \widetilde{\mathcal{W}}_{\mathbf{k}',\mathbf{k}}(1 - \cos \theta' \cos \varphi'), \quad (42)$$

$$\Gamma_{\text{tr}}^z = \frac{1}{\tau_{\text{tr}}^z} = \frac{\kappa_F k_0}{(2\pi)^3 v_0} \int d\varphi' d\theta' \widetilde{\mathcal{W}}_{\mathbf{k}',\mathbf{k}}(1 - \cos \varphi'). \quad (43)$$

The angular factors in Eqs. (42) and (43) are Ziman transport factors [38], adapted to the toroidal geometry: they suppress forward-scattering processes that do not

	Γ	Γ_{tr}^i
$T \ll T_{\text{BG}}^{(\text{pol})}$	T^3	T^5
$T_{\text{BG}}^{(\text{pol})} \ll T \ll T_{\text{BG}}^{(\text{tor})}$	T^2	T^2
$T_{\text{BG}}^{(\text{tor})} \ll T$	T	T

Table I. Temperature dependence of the decay rate Γ and the scattering rates Γ_{tr}^i ($i = x, y, z$) for quasiparticles on the Fermi surface. The corresponding resistivity behaves as $\rho \propto T^5$ for $T \ll T_{\text{BG}}^{(\text{pol})}$, $\rho \propto T^2$ in the intermediate regime $T_{\text{BG}}^{(\text{pol})} \ll T \ll T_{\text{BG}}^{(\text{tor})}$, and $\rho \propto T$ at $T \gg T_{\text{BG}}^{(\text{tor})}$, mirroring the standard BG behavior at low and high temperatures and the torus-induced intermediate scaling.

efficiently relax the current along a given direction and weight more heavily momentum transfers that strongly deflect the velocity vector on the Fermi torus. This directional dependence produces the anisotropy between in-plane (x, y) and the axial (z) transport lifetimes. The anisotropy originates from the Fermi-surface geometry and is distinct from the material-dependent anisotropy of the energy dispersion close to the nodal line, which we neglect here (we set the dispersion anisotropy parameter $\alpha = 1$).

We use Eqs. (42) and (43) to evaluate the conductivity in Sec. V.

IV. QUASIPARTICLE DECAY RATE

Before analyzing the conductivity, we evaluate the temperature dependence of the single-particle decay rate $\Gamma_{\mathbf{k}}(T)$, which can be accessed experimentally through the linewidth of ARPES peaks [4, 36, 37, 57, 58]. The decay rate follows from the out-scattering term of the BTE (33) and it is given by

$$\Gamma_{\mathbf{k}} = \int \frac{d^3\mathbf{k}'}{(2\pi)^3} \mathcal{W}_{\mathbf{k}',\mathbf{k}}. \quad (44)$$

Under the approximations discussed in Sec. III, $\Gamma_{\mathbf{k}}$ can be expressed as the Fermi surface integral

$$\Gamma = \frac{g_0^2 \kappa_F k_0}{(2\pi)^2 \rho_M c_l v_0} \int d\varphi' d\theta' \frac{|\mathbf{q}|}{\sinh(\beta c_l |\mathbf{q}|)} \cos^2\left(\frac{\varphi - \varphi'}{2}\right), \quad (45)$$

where the modulus of the momentum transfer $|\mathbf{q}|$ is given in Eq. (38), and we have used the spinor overlap from Eq. (11). Since the integrand only depends on angle differences, $\Gamma_{\mathbf{k}}$ is uniform over the Fermi surface up to $\mathcal{O}(\kappa_F/k_0)$ corrections, and we henceforth drop the \mathbf{k} label. We then shift the integration variables and, using periodicity and reflection symmetry, restrict the integration domain. With the substitutions $\theta', \varphi' \rightarrow 2\theta' + \theta, 2\varphi' + \varphi$, we arrive at the compact expression

$$\Gamma = \frac{8g_0^2 \kappa_F k_0}{\pi^2 \rho_M c_l v_0} \int_0^{\frac{\pi}{2}} d\varphi' \int_0^{\frac{\pi}{2}} d\theta' \frac{Q(\theta', \varphi') \cos^2(\varphi')}{\sinh[2\beta c_l Q(\theta', \varphi')]}, \quad (46)$$

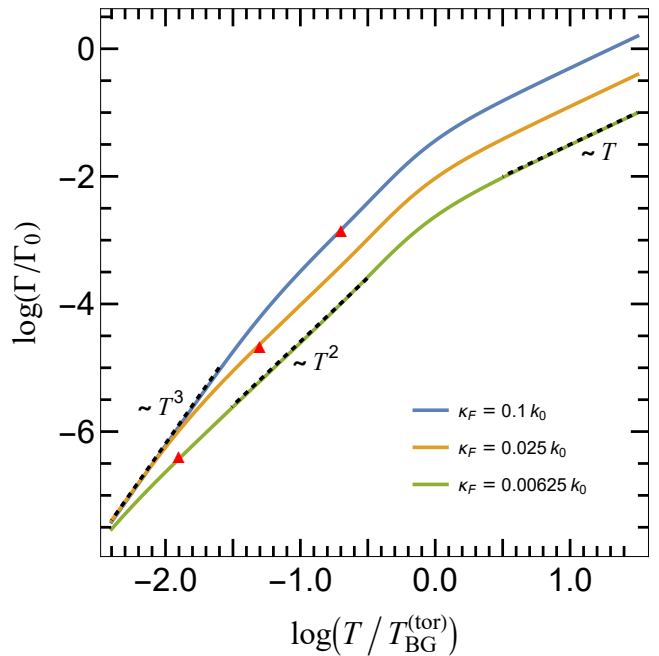


Figure 2. Temperature dependence of the quasiparticle decay rate $\Gamma(T)$ obtained from a direct numerical evaluation of Eq. (45). Results are shown for $c_l/v_0 = 10^{-2}$ and for several chemical potentials (see legend), with Γ_0 defined in Eq. (49). The red markers indicate $T = T_{\text{BG}}^{(\text{pol})}$. Dashed black lines represent asymptotic power-law fits across the three temperature regimes.

where we have defined

$$Q(\theta, \varphi) = \sqrt{k_0^2 \sin^2(\theta) + \kappa_F^2 \sin^2(\varphi)}. \quad (47)$$

As discussed in Sec. IID, the thin-torus limit $\kappa_F \ll k_0$ implies two BG temperature scales, $T_{\text{BG}}^{(\text{pol})} \propto \kappa_F$ and $T_{\text{BG}}^{(\text{tor})} \propto k_0$, and therefore three temperature regimes. The evaluation of Eq. (46) in these regimes is presented in Appendix D; here we summarize the resulting power laws in Table I and provide simple phase-space arguments for the scalings. For $T \ll T_{\text{BG}}^{(\text{pol})}$, both angular separations are restricted by the thermal bound $Q \lesssim k_B T / 2c_l$, giving $\Delta\theta \sim k_B T / (2c_l k_0)$ and $\Delta\varphi \sim k_B T / (2c_l \kappa_F)$. Hence the available phase space scales as $\Delta\theta \Delta\varphi \propto T^2$. Together with the explicit factor $Q \sim T$ in Eq. (46), this gives $\Gamma \propto T^3$.

In the intermediate window $T_{\text{BG}}^{(\text{pol})} \ll T \ll T_{\text{BG}}^{(\text{tor})}$, poloidal momentum transfers of order κ_F are thermally allowed, while the large toroidal radius k_0 forces the toroidal angular separation to be small in order to keep $Q \lesssim k_B T / 2c_l$: $\Delta\theta \sim Q/k_0 \sim k_B T / (2c_l k_0) \propto T$. Equation (46) provides one explicit factor $Q \sim T$, and together with the restriction $\Delta\theta \propto T$, makes the available phase space on the torus $\Delta\theta \Delta\varphi \propto T$, yielding $\Gamma \propto T^2$.

For $T \gg T_{\text{BG}}^{(\text{tor})}$, the angular phase space saturates, and the leading temperature dependence arises from

$1/\sinh x \simeq 1/x$ for small $x = 2\beta c_l Q$ in Eq. (46), yielding the scattering rate proportional to the number of phonons available for scattering, i.e., $\Gamma \propto T$.

More explicitly, we obtain the following asymptotic power laws for quasiparticles at the Fermi level ($\varepsilon = \mu$), derived in Appendix D. In the low temperature regime, $T \ll T_{\text{BG}}^{(\text{pol})}$, the decay rate follows

$$\Gamma = \frac{7\zeta(3)}{4\pi} \Gamma_0 \left(\frac{T}{T_{\text{BG}}^{(\text{tor})}} \right)^3, \quad (48)$$

where $\zeta(s)$ is the Riemann zeta function and

$$\Gamma_0 = \frac{g_0^2 k_0^3}{\rho_M c_l v_0}. \quad (49)$$

sets the characteristic electron-phonon scattering scale. In the intermediate regime we find

$$\Gamma = \frac{\pi}{16} \Gamma_0 \left(\frac{T_{\text{BG}}^{(\text{pol})}}{T_{\text{BG}}^{(\text{tor})}} \right) \left(\frac{T}{T_{\text{BG}}^{(\text{tor})}} \right)^2, \quad (50)$$

and finally in the high-temperature regime

$$\Gamma = \frac{1}{4} \Gamma_0 \left(\frac{T_{\text{BG}}^{(\text{pol})}}{T_{\text{BG}}^{(\text{tor})}} \right) \left(\frac{T}{T_{\text{BG}}^{(\text{tor})}} \right), \quad (51)$$

the standard high-temperature linear-in- T dependence [39]. Figure 2 shows a direct numerical evaluation of Eq. (45), confirming the three scaling regimes and power laws summarized in Table I.

V. CONDUCTIVITY

Having established the temperature dependence of the quasiparticle decay rate $\Gamma(T)$, we now turn our attention to the dc conductivity, which is controlled by the transport lifetimes introduced in Sec. III.

The electric current density is

$$\mathbf{J} = e \int \frac{d^3\mathbf{k}}{(2\pi)^3} \mathbf{v}(\mathbf{k}) f_{\mathbf{k}}. \quad (52)$$

Inserting Eq. (30) together with Eq. (39), the equilibrium contribution vanishes by symmetry, yielding

$$\mathbf{J} = -e^2 \int \frac{d^3\mathbf{k}}{(2\pi)^3} \mathbf{v}(\mathbf{k}) (\mathbf{E} \cdot \mathbf{\Lambda}_{\mathbf{k}}) \frac{\partial n_{\text{F}}(\varepsilon_{\mathbf{k}})}{\partial \varepsilon_{\mathbf{k}}}. \quad (53)$$

Using the BTE solution (41) and identifying $\mathbf{J} = \boldsymbol{\sigma} \mathbf{E}$, we obtain for the conductivity tensor

$$\sigma_{ij} = \frac{e^2 \kappa_{\text{F}} k_0 \tau_{\text{tr}}^j}{(2\pi)^3} \int d\varphi d\theta e_{\kappa}^i e_{\kappa}^j, \quad (54)$$

which yields the longitudinal conductivities

$$\sigma_{xx} = \sigma_{yy} = \frac{e^2 \tau_{\text{tr}}^x \mu k_0}{8\pi}, \quad \sigma_{zz} = \frac{e^2 \tau_{\text{tr}}^z \mu k_0}{4\pi}, \quad (55)$$

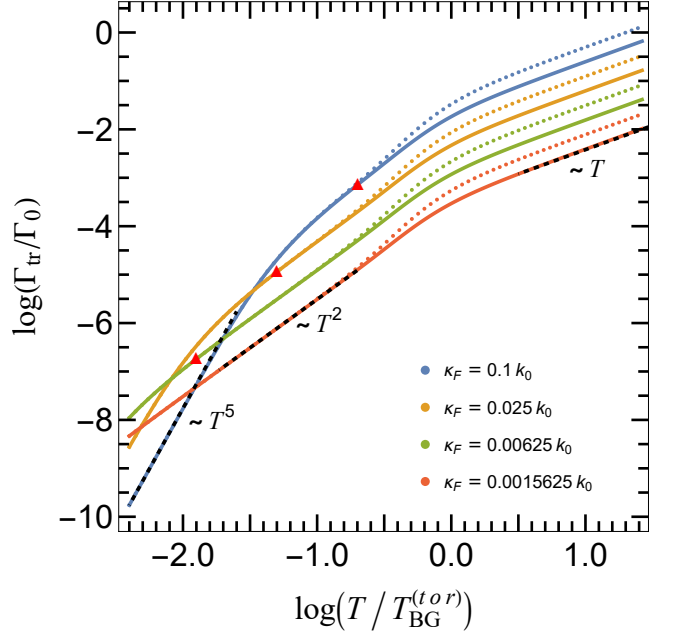


Figure 3. Temperature dependence of the transport scattering rates $\Gamma_{\text{tr}}^z(T)$ (solid line) and $\Gamma_{\text{tr}}^x(T)$ (dotted line) obtained from direct numerical evaluation of Eqs. (56) and (57). Results are shown for $c_l/v_0 = 10^{-2}$ and for several chemical potentials (see legend), with Γ_0 defined in Eq. (49). The red markers indicate $T = T_{\text{BG}}^{(\text{pol})}$. Note that for the red curve, the poloidal BG temperature $T_{\text{BG}}^{(\text{pol})}$ falls outside the temperature window displayed. Dashed black lines represent asymptotic power-law fits across the three temperature regimes.

while the off-diagonal terms vanish by symmetry. From this expression, we see that the temperature dependence of the conductivity is set by transport lifetimes τ_{tr}^i given in Eqs. (42) and (43).

With manipulations similar to those leading to Eq. (46) we obtain

$$\Gamma_{\text{tr}}^x = \frac{8g_0^2 k_0 \kappa_{\text{F}}}{\pi^2 \rho_M c_l v_0} \int_0^{\frac{\pi}{2}} d\varphi' \int_0^{\frac{\pi}{2}} d\theta' \frac{Q(\theta', \varphi') \cos^2(\varphi')}{\sinh[2\beta c_l Q(\theta', \varphi')]} \times [1 - \cos(2\varphi') \cos(2\theta')], \quad (56)$$

$$\Gamma_{\text{tr}}^z = \frac{8g_0^2 k_0 \kappa_{\text{F}}}{\pi^2 \rho_M c_l v_0} \int_0^{\frac{\pi}{2}} d\varphi' \int_0^{\frac{\pi}{2}} d\theta' \frac{Q(\theta', \varphi') \cos^2(\varphi')}{\sinh[2\beta c_l Q(\theta', \varphi')]} \times [1 - \cos(2\varphi')], \quad (57)$$

with $Q(\theta, \varphi)$ defined in Eq. (47). In Appendix E we analytically evaluate Eqs. (56) and (57), obtaining the temperature dependences summarized in Table I. We see a clear agreement between the transport scattering rate results of Table I and the numerics in Fig. 3. We find that the temperature dependence of the transport scattering

rate at low temperature follows

$$\Gamma_{\text{tr}}^x = \Gamma_{\text{tr}}^z = \frac{93\zeta(5)}{4\pi} \Gamma_0 \left(\frac{T_{\text{BG}}^{(\text{tor})}}{T_{\text{BG}}^{(\text{pol})}} \right)^2 \left(\frac{T}{T_{\text{BG}}^{(\text{tor})}} \right)^5, \quad (58)$$

where $\zeta(5) \simeq 1.037$. This T^5 temperature dependence of the rate implies $\sigma_{ii} \propto T^{-5}$ for the conductivities, which is the standard low-temperature behavior in conventional metals [38]. At intermediate temperatures, similar to Eq. (50), we get

$$\Gamma_{\text{tr}}^x = \Gamma_{\text{tr}}^z = \frac{\pi}{32} \Gamma_0 \left(\frac{T_{\text{BG}}^{(\text{pol})}}{T_{\text{BG}}^{(\text{tor})}} \right) \left(\frac{T}{T_{\text{BG}}^{(\text{tor})}} \right)^2. \quad (59)$$

In this regime, only $\Delta\theta \propto T$ while $\Delta\varphi$ spans the whole integration domain. As a result, the angular transport weighting factors in Eqs. (56) and (57) contribute at $\mathcal{O}(1)$, yielding the same T^2 dependence for the transport scattering rate as for the decay rate. Finally, in the high temperature regime $T \gg T_{\text{BG}}^{(\text{tor})}$, we find

$$\Gamma_{\text{tr}}^z = \frac{\Gamma_{\text{tr}}^x}{2} = \frac{1}{8} \Gamma_0 \left(\frac{T_{\text{BG}}^{(\text{pol})}}{T_{\text{BG}}^{(\text{tor})}} \right) \left(\frac{T}{T_{\text{BG}}^{(\text{tor})}} \right), \quad (60)$$

i.e., a linear-in- T dependence. From Eq. (55), we thus find that

$$\frac{\sigma_{zz}}{\sigma_{xx}} = 2, \quad T \ll T_{\text{BG}}^{(\text{tor})}, \quad (61)$$

$$\frac{\sigma_{zz}}{\sigma_{xx}} = 4, \quad T \gg T_{\text{BG}}^{(\text{tor})}. \quad (62)$$

The increase of the conductivity anisotropy upon raising the temperature through $T_{\text{BG}}^{(\text{tor})}$ is a direct consequence of the toroidal Fermi-surface geometry.

VI. SUMMARY AND OUTLOOK

In this work, we have analyzed quasiparticle scattering and charge transport in doped NLSs with a toroidal Fermi surface, focusing on longitudinal acoustic phonons coupled to electrons via a deformation potential. Using a low-energy two-band model with a circular nodal ring, we consider the regime below the Lifshitz scale, where the Fermi surface is a thin torus characterized by a major radius k_0 and a minor radius κ_F . This geometry gives rise to two parametrically distinct BG temperature scales, $T_{\text{BG}}^{(\text{pol})} \propto c_l \kappa_F$ and $T_{\text{BG}}^{(\text{tor})} \propto c_l k_0$, associated with phonons probing the poloidal and toroidal dimensions of the Fermi surface, respectively. Using Fermi's golden rule and the linearized BTE (which we solved exactly to leading order in κ_F/k_0), we found that the quasiparticle decay rate and the conductivity exhibit three temperature regimes: the low- and high-temperature limits reproduce the familiar BG behavior, while the intermediate T^2/T^{-2} scaling emerges from the toroidal Fermi surface and the separation of the momentum scales κ_F and k_0 . Corrections of

order κ_F/k_0 break translational invariance on the torus and lead to additional angular harmonics in the collision kernel. However, we expect these subleading terms only renormalize the eigenvalues of the collision operator by $\mathcal{O}(\kappa_F/k_0)$ and therefore are not expected to modify the power-law exponents of the leading terms that we obtain in the strict thin-torus limit.

The origin of the modified scaling can be traced to the phase-space measure. For a spherical Fermi surface, the kinematic constraint $|\mathbf{q}| \lesssim T$ restricts both angular directions, giving a phase-space measure $\Delta\Omega \sim (\Delta\theta)^2 \sim T^2$. Combined with the typical momentum transfer $|\mathbf{q}| \sim T$ and the transport weighting factor $(1 - \cos\theta) \sim T^2$, this yields the conventional low-temperature Bloch-Grüneisen scaling $\propto T^5$. In contrast, for a toroidal Fermi surface in the thin-torus limit, the phase space measure factorizes as $\Delta\theta \Delta\varphi$, with $\Delta\theta \sim T$ while $\Delta\varphi$ spans the full integration domain in the intermediate regime. Together with $|\mathbf{q}| \sim T$ and transport weighting factors that contribute at $\mathcal{O}(1)$, this leads to the parametrically distinct T^2 scaling obtained here.

Our predictions can be tested experimentally. The quasiparticle decay rate is accessible in ARPES experiments as a linewidth, and in materials with a toroidal Fermi surface and linear dispersion along the minor-radius direction, we predict an intermediate window where $\Gamma \propto T^2$. The corresponding temperature dependence of the transport lifetime, and thus the conductivity, can be probed via standard four-probe measurements, for which we predict $\sigma \propto T^{-2}$, i.e., a resistivity $\rho \propto T^2$ in the same regime. Importantly, the onset of this intermediate regime is controlled by $T_{\text{BG}}^{(\text{pol})} \propto \kappa_F \propto \mu$, so tuning the chemical potential should shift the lower crossover temperature, providing a direct way to distinguish this phonon mechanism from other sources of T^2 resistivity. While a T^2 resistivity is commonly attributed to intra-band electron-electron scattering [39, 48], our results show that in NLSs with a toroidal Fermi surface, a purely electron-phonon mechanism can generate the same temperature dependence.

We also find that the Fermi-surface geometry leads to an enhanced conductivity anisotropy in the high-temperature regime. We emphasize that, in the thin-torus limit, circular nodal-line semimetals exhibit an intrinsically anisotropic transport lifetime. Even when the scattering kernel depends only on angular differences, isotropic treatments are inadequate, and the transport lifetime must instead be evaluated using Eqs. (42) and (43).

One of the key assumptions of our model is the absence of energy dispersion along the nodal line, i.e., the nodal line is assumed to be flat in energy. In general, no crystal symmetry enforces such flatness, and consequently most nodal-line semimetals do not exhibit simple toroidal Fermi surfaces. Instead, more complicated geometries such as Dupin cyclides [59] arise, to which our analysis does not directly apply, since a clear separation between poloidal and toroidal radii is not pos-

sible and interband scattering between coexisting electron and hole pockets may become important. While materials such as CaAgAs [60] have been proposed to host nearly toroidal (donut-like) hole Fermi surface — serving as a “hydrogen atom” realization of a nodal-line semimetal — in many materials, such as ZrSiS, achieving a purely toroidal Fermi surface imposes a lower bound on the achievable carrier density [16, 30].

In materials hosting additional trivial Fermi pockets or multiple nodal loops, these channels will contribute parallel conduction paths with their own, typically single-scale BG behavior. Nevertheless, as long as a toroidal pocket with $\kappa_F \ll k_0$ remains well defined and dominates the low-energy density of states, the two-scale structure and the intermediate T^2/T^{-2} regime should survive as robust features of the total response.

Several refinements and extensions are left for future work, such as including crystal anisotropy, energy-dispersive or non-circular nodal lines, additional Fermi pockets, and analysing how they renormalize prefactors and/or shift the crossover scales $T_{\text{BG}}^{(\text{pol})}$, $T_{\text{BG}}^{(\text{tor})}$. We expect the existence of two BG scales and an intermediate T^2/T^{-2} window to be a generic consequence of Fermi surfaces with two widely separated characteristic momenta, even when the assumptions of an ideal circular nodal ring and a perfectly isotropic elastic medium considered here are relaxed. By contrast, quantitative features such as the precise values $\sigma_{zz}/\sigma_{xx} = 2$ at low T and 4 at high T are geometry-specific and will be modified by crystal anisotropy and additional pockets. It would also be in-

teresting to extend our study to thermal transport and thermoelectric response, by evaluating the corresponding Boltzmann integrals for the heat current and extracting the temperature dependence of the thermal conductivity and the Seebeck coefficient across the two BG scales. Including impurity and electron-electron scattering on an equal footing would enable a more quantitative comparison with experiments on specific materials.

ACKNOWLEDGMENTS

We acknowledge helpful discussions with F. Buccheri, R. Citro, and R. Egger. A.A. is grateful for the PhD studentship provided by the School of Science and Technology, City St Georges, University of London.

DATA AVAILABILITY

The data underlying the figures in this paper are available in Zenodo [61].

Appendix A: Linearized Boltzmann equation

In this Appendix, we outline the derivation of the linearized BTE (33). Substituting the transition rates (21) into Eq. (29), we can write the integrand of the collision integral (29) as

$$\begin{aligned} \mathcal{C}_{\mathbf{k},\mathbf{k}'} &\equiv W_{\mathbf{k},\mathbf{k}'} f_{\mathbf{k}'}(1 - f_{\mathbf{k}}) - W_{\mathbf{k}',\mathbf{k}} f_{\mathbf{k}}(1 - f_{\mathbf{k}'}), \\ &= 2\pi |\mathcal{G}_{\mathbf{k},\mathbf{k}'}|^2 \left\{ n_{\text{B}}(\Omega_{\mathbf{q}}) f_{\mathbf{k}'}(1 - f_{\mathbf{k}}) \delta(\varepsilon_{\mathbf{k}} - \varepsilon_{\mathbf{k}'} - \Omega_{\mathbf{q}}) + [n_{\text{B}}(\Omega_{\mathbf{q}}) + 1] f_{\mathbf{k}'}(1 - f_{\mathbf{k}}) \delta(\varepsilon_{\mathbf{k}} - \varepsilon_{\mathbf{k}'} + \Omega_{\mathbf{q}}) \right. \\ &\quad \left. - n_{\text{B}}(\Omega_{\mathbf{q}}) f_{\mathbf{k}}(1 - f_{\mathbf{k}'}) \delta(\varepsilon_{\mathbf{k}'} - \varepsilon_{\mathbf{k}} - \Omega_{\mathbf{q}}) - [n_{\text{B}}(\Omega_{\mathbf{q}}) + 1] f_{\mathbf{k}}(1 - f_{\mathbf{k}'}) \delta(\varepsilon_{\mathbf{k}'} - \varepsilon_{\mathbf{k}} + \Omega_{\mathbf{q}}) \right\}, \end{aligned} \quad (\text{A1})$$

where we have used the symmetry $|\mathcal{G}_{\mathbf{k},\mathbf{k}'}| = |\mathcal{G}_{\mathbf{k}',\mathbf{k}}|$. Grouping terms with the same delta-function argument and linearizing the distribution function using Eq. (30), we obtain

$$\begin{aligned} \mathcal{C}_{\mathbf{k},\mathbf{k}'} &= 2\pi |\mathcal{G}_{\mathbf{k},\mathbf{k}'}|^2 \left\{ \left[(n_{\text{B}}(\Omega_{\mathbf{q}}) + 1 - n_{\text{F}}(\varepsilon_{\mathbf{k}'})) \varphi_{\mathbf{k}} \frac{\partial n_{\text{F}}(\varepsilon_{\mathbf{k}})}{\partial \varepsilon_{\mathbf{k}}} - (n_{\text{B}}(\Omega_{\mathbf{q}}) + n_{\text{F}}(\varepsilon_{\mathbf{k}})) \varphi_{\mathbf{k}'} \frac{\partial n_{\text{F}}(\varepsilon_{\mathbf{k}'})}{\partial \varepsilon_{\mathbf{k}'}} \right] \delta(\varepsilon_{\mathbf{k}'} - \varepsilon_{\mathbf{k}} + \Omega_{\mathbf{q}}) \right. \\ &\quad \left. + \left[(n_{\text{B}}(\Omega_{\mathbf{q}}) + n_{\text{F}}(\varepsilon_{\mathbf{k}'})) \varphi_{\mathbf{k}} \frac{\partial n_{\text{F}}(\varepsilon_{\mathbf{k}})}{\partial \varepsilon_{\mathbf{k}}} - (n_{\text{B}}(\Omega_{\mathbf{q}}) + 1 - n_{\text{F}}(\varepsilon_{\mathbf{k}})) \varphi_{\mathbf{k}'} \frac{\partial n_{\text{F}}(\varepsilon_{\mathbf{k}'})}{\partial \varepsilon_{\mathbf{k}'}} \right] \delta(\varepsilon_{\mathbf{k}'} - \varepsilon_{\mathbf{k}} - \Omega_{\mathbf{q}}) \right\}, \end{aligned} \quad (\text{A2})$$

where the zeroth-order terms cancel by detailed balance. Next, we use the two identities

$$[n_{\text{B}}(\Omega_{\mathbf{q}}) + n_{\text{F}}(\varepsilon_{\mathbf{k}})] \frac{\partial n_{\text{F}}(\varepsilon_{\mathbf{k}'})}{\partial \varepsilon_{\mathbf{k}'}} = [n_{\text{B}}(\Omega_{\mathbf{q}}) + 1 - n_{\text{F}}(\varepsilon_{\mathbf{k}'})] \frac{\partial n_{\text{F}}(\varepsilon_{\mathbf{k}})}{\partial \varepsilon_{\mathbf{k}}}, \quad \text{when } \varepsilon_{\mathbf{k}'} = \varepsilon_{\mathbf{k}} - \Omega_{\mathbf{q}}, \quad (\text{A3})$$

$$[n_{\text{B}}(\Omega_{\mathbf{q}}) + 1 - n_{\text{F}}(\varepsilon_{\mathbf{k}})] \frac{\partial n_{\text{F}}(\varepsilon_{\mathbf{k}'})}{\partial \varepsilon_{\mathbf{k}'}} = [n_{\text{B}}(\Omega_{\mathbf{q}}) + n_{\text{F}}(\varepsilon_{\mathbf{k}'})] \frac{\partial n_{\text{F}}(\varepsilon_{\mathbf{k}})}{\partial \varepsilon_{\mathbf{k}}}, \quad \text{when } \varepsilon_{\mathbf{k}'} = \varepsilon_{\mathbf{k}} + \Omega_{\mathbf{q}}, \quad (\text{A4})$$

and recast Eq. (A2) into the form

$$\begin{aligned} \mathcal{C}_{\mathbf{k},\mathbf{k}'} &= 2\pi |\mathcal{G}_{\mathbf{k},\mathbf{k}'}|^2 \frac{\partial n_{\text{F}}(\varepsilon_{\mathbf{k}})}{\partial \varepsilon_{\mathbf{k}}} \left\{ [n_{\text{B}}(\Omega_{\mathbf{q}}) + 1 - n_{\text{F}}(\varepsilon_{\mathbf{k}'})] \delta(\varepsilon_{\mathbf{k}'} - \varepsilon_{\mathbf{k}} + \Omega_{\mathbf{q}}) + [n_{\text{B}}(\Omega_{\mathbf{q}}) + n_{\text{F}}(\varepsilon_{\mathbf{k}'})] \delta(\varepsilon_{\mathbf{k}'} - \varepsilon_{\mathbf{k}} - \Omega_{\mathbf{q}}) \right\} (\varphi_{\mathbf{k}} - \varphi_{\mathbf{k}'}) \\ &= \frac{\partial n_{\text{F}}(\varepsilon_{\mathbf{k}})}{\partial \varepsilon_{\mathbf{k}}} \mathcal{W}_{\mathbf{k}',\mathbf{k}}(\varphi_{\mathbf{k}} - \varphi_{\mathbf{k}'}), \end{aligned} \quad (\text{A5})$$

with the kernel $\mathcal{W}_{\mathbf{k}',\mathbf{k}}$ given in Eq. (32).

We can now write the BTE (28) to first order in the deviation from equilibrium as

$$e\mathbf{E} \cdot \partial_{\mathbf{k}} n_{\text{F}}(\varepsilon_{\mathbf{k}}) = \int \frac{d^3\mathbf{k}'}{(2\pi)^3} \mathcal{C}_{\mathbf{k},\mathbf{k}'}. \quad (\text{A6})$$

Substituting Eq. (A5) in Eq. (A6), we finally get

$$e\mathbf{E} \cdot \mathbf{v}(\mathbf{k}) = \mathcal{J}_{\mathbf{k}}, \quad (\text{A7})$$

where $\mathcal{J}_{\mathbf{k}}$ is defined in Eq. (31).

Appendix B: Solution of the BTE

In this Appendix, we present the solution of the linearized BTE (40). The equation can be cast in the form

$$e_{\kappa}^i(\theta, \varphi) = \int d\theta' d\varphi' K(\theta, \varphi; \theta', \varphi') [\Lambda^i(\theta, \varphi) - \Lambda^i(\theta', \varphi')], \quad (\text{B1})$$

where the kernel $K(\theta, \varphi; \theta', \varphi')$ is given by

$$K(\theta, \varphi; \theta', \varphi') = \frac{\kappa_{\text{F}} k_0}{(2\pi)^3 v_0^2} \widetilde{\mathcal{W}}_{\mathbf{k}',\mathbf{k}}, \quad (\text{B2})$$

and the angles (θ, φ) and (θ', φ') parametrize the momenta \mathbf{k} and \mathbf{k}' on the Fermi surface. As discussed in the main text, in the thin-torus limit, the kernel depends only on angle differences:

$$K(\theta, \varphi; \theta', \varphi') = f(\theta - \theta', \varphi - \varphi'), \quad (\text{B3})$$

where $f(\theta, \varphi)$ is a real function even in both arguments. As a consequence, the integral operator in Eq. (B1) takes the form of a convolution, and the equation can be solved by Fourier transform.

Expanding e_{κ}^i , Λ^i , and f in a double Fourier series as

$$e_{\kappa}^i(\theta, \varphi) = \sum_{m,n \in \mathbb{Z}} e_{\kappa,mn}^i e^{im\theta + in\varphi}, \quad (\text{B4})$$

$$\Lambda^i(\theta, \varphi) = \sum_{m,n \in \mathbb{Z}} \Lambda_{mn}^i e^{im\theta + in\varphi}, \quad (\text{B5})$$

$$f(\theta, \varphi) = \sum_{m,n \in \mathbb{Z}} f_{mn} e^{im\theta + in\varphi}, \quad (\text{B6})$$

and substituting the Fourier expansions into Eq. (B1) yields

$$e_{\kappa,mn}^i = (2\pi)^2 (f_{00} - f_{mn}) \Lambda_{mn}^i, \quad (\text{B7})$$

and thus

$$\Lambda_{mn}^i = \frac{e_{\kappa,mn}^i}{(2\pi)^2 (f_{00} - f_{mn})}. \quad (\text{B8})$$

Since e_{κ}^i are simple trigonometric functions (see Eq. (13)), only a few Fourier coefficients are non-vanishing. Then, using the even parity of f :

$$f_{m,n} = f_{-m,n} = f_{m,-n} = f_{-m,-n}, \quad (\text{B9})$$

we arrive at

$$\Lambda^i(\theta, \varphi) = \frac{e_{\kappa}^i(\theta, \varphi)}{(2\pi)^2 (f_{00} - f_{11})}, \quad i = x, y \quad (\text{B10})$$

$$\Lambda^z(\theta, \varphi) = \frac{e_{\kappa}^z(\theta, \varphi)}{(2\pi)^2 (f_{00} - f_{01})}. \quad (\text{B11})$$

where

$$f_{mn} = \int \frac{d\varphi d\theta}{(2\pi)^2} f(\theta, \varphi) \cos(m\theta) \cos(n\varphi). \quad (\text{B12})$$

This yields the transport lifetime expressions in Eqs. (42) and (43).

Appendix C: Momentum transfer

In this Appendix, we derive the thin-torus expression for the magnitude of the momentum transfer between two states on the toroidal Fermi surface, Eq. (38). Using the parameterization in Eqs. (6)–(8), the momentum transfer $\mathbf{q} = \mathbf{k}' - \mathbf{k}$ can be decomposed as

$$\mathbf{q} = \mathbf{q}_0 + \mathbf{q}' \quad (\text{C1})$$

where the major-radius contribution is

$$\mathbf{q}_0 = k_0 (\cos \theta' - \cos \theta) \hat{x} + k_0 (\sin \theta' - \sin \theta) \hat{y}, \quad (\text{C2})$$

and the minor-radius correction reads

$$\mathbf{q}' = \kappa_{\text{F}} (\cos \varphi' \cos \theta' - \cos \varphi \cos \theta) \hat{x} + \kappa_{\text{F}} (\cos \varphi' \sin \theta' - \cos \varphi \sin \theta) \hat{y} + \kappa_{\text{F}} (\sin \varphi' - \sin \varphi) \hat{z}. \quad (\text{C3})$$

A straightforward algebra then gives

$$\begin{aligned} |\mathbf{q}|^2 &= 4k_0^2 \sin^2 \left(\frac{\theta - \theta'}{2} \right) \left[1 + \frac{1}{2} \frac{\kappa_{\text{F}}}{k_0} (\cos \varphi' + \cos \varphi) + \left(\frac{\kappa_{\text{F}}}{k_0} \right)^2 \cos \varphi' \cos \varphi \right] + 4\kappa_{\text{F}}^2 \sin^2 \left(\frac{\varphi - \varphi'}{2} \right). \end{aligned} \quad (\text{C4})$$

To leading order in $\kappa_F/k_0 \ll 1$ we may drop the terms in square brackets beyond unity, which leads to Eq. (38).

Appendix D: Decay rate

In this Appendix, we present details of the analytical evaluation of the quasiparticle decay rate discussed in Sec. IV. We use Eq. (46) to extract asymptotic forms of $\Gamma(T)$ in the relevant temperature regimes.

1. Low temperature

In the regime $T \ll T_{\text{BG}}^{(\text{pol})}$, i.e., $\beta c_l k_0 \gg \beta c_l \kappa_F \gg 1$, the factor $1/\sinh(2\beta c_l Q)$ in Eq. (46) exponentially suppresses contributions from all but the smallest momentum transfers. Hence, the dominant contribution arises from the vicinity $\theta', \varphi' \simeq 0$, where we may linearize the sine terms by using $\sin x \simeq x$ and set $\cos \varphi' \simeq 1$. This yields

$$\Gamma = B \int_0^{\frac{\pi}{2}} d\varphi' \int_0^{\frac{\pi}{2}} d\theta' \frac{\sqrt{k_0^2 \theta'^2 + \kappa_F^2 \varphi'^2}}{\sinh\left(2\beta c_l \sqrt{k_0^2 \theta'^2 + \kappa_F^2 \varphi'^2}\right)}, \quad (\text{D1})$$

with

$$B = \frac{8g_0^2 \kappa_F k_0}{\pi^2 \rho_M c_l v_0}. \quad (\text{D2})$$

Introducing the dimensionless variables

$$x = 2\beta c_l k_0 \theta', \quad y = 2\beta c_l \kappa_F \varphi', \quad (\text{D3})$$

we obtain

$$\Gamma = \frac{B}{(2\beta c_l)^3 \kappa_F k_0} \int_0^{\beta c_l \kappa_F \pi} dy \int_0^{\beta c_l k_0 \pi} dx \frac{\sqrt{x^2 + y^2}}{\sinh \sqrt{x^2 + y^2}}. \quad (\text{D4})$$

Since $\beta c_l k_0, \beta c_l \kappa_F \gg 1$, the upper integration limits can be extended to ∞ . Switching to polar coordinates then gives

$$\Gamma = \frac{B}{(2\beta c_l)^3 \kappa_F k_0} \frac{\pi}{2} \int_0^\infty dr \frac{r^2}{\sinh r}. \quad (\text{D5})$$

Using the standard integral $\int_0^\infty dr r^2 / \sinh r = \frac{7}{2}\zeta(3)$, we finally obtain Eq. (48).

2. Intermediate temperature

In the intermediate regime $T_{\text{BG}}^{(\text{pol})} \ll T \ll T_{\text{BG}}^{(\text{tor})}$, i.e., $\beta c_l k_0 \gg 1 \gg \beta c_l \kappa_F$, we may still linearize $\sin \theta'$ but not $\sin \varphi'$. Using Eq. (D3) in Eq. (46) gives

$$\Gamma = \frac{B}{(2\beta c_l)^2 k_0} \int_0^{\frac{\pi}{2}} d\varphi' \int_0^{\beta c_l k_0 \pi} dx \frac{\cos^2(\varphi') \sqrt{x^2 + b^2(\varphi')}}{\sinh \sqrt{x^2 + b^2(\varphi')}}}, \quad (\text{D6})$$

where $b(\varphi') = 2\beta c_l \kappa_F \sin(\varphi')$. To lowest order in κ_F/k_0 we may set $b(\varphi') \simeq 0$, and since $\beta c_l k_0 \gg 1$ we extend the upper limit of the x integral to ∞ . This gives

$$\Gamma = \frac{B}{(2\beta c_l)^2 k_0} \int_0^{\frac{\pi}{2}} d\varphi' \cos^2(\varphi') \int_0^\infty dx \frac{x}{\sinh x}. \quad (\text{D7})$$

Using $\int_0^\infty dx x / \sinh x = \frac{\pi^2}{4}$ and $\int_0^{\pi/2} d\varphi' \cos^2 \varphi' = \pi/4$, we finally obtain Eq. (50).

3. High temperature

Finally, in the regime $T_{\text{BG}}^{(\text{pol})} \ll T_{\text{BG}}^{(\text{tor})} \ll T$, i.e., $1 \gg \beta c_l k_0 \gg \beta c_l \kappa_F$, we may linearize the denominator in Eq. (46) obtaining

$$\Gamma = B \int_0^{\frac{\pi}{2}} d\varphi' \cos^2(\varphi') \int_0^{\frac{\pi}{2}} d\theta' \frac{1}{2\beta c_l}, \quad (\text{D8})$$

which immediately gives Eq. (51).

Appendix E: Transport lifetimes

In this Appendix, we evaluate Eqs. (56) and (57) in the three temperature regimes, following the same procedure as in Appendix D.

1. Low temperature

When $T \ll T_{\text{BG}}^{(\text{pol})}$, we expand the trigonometric functions to lowest order, obtaining ($i = x, y, z$)

$$\Gamma_{\text{tr}}^i = 2B \int_0^{\frac{\pi}{2}} d\varphi' \int_0^{\frac{\pi}{2}} d\theta' \frac{(\varphi'^2 + a_i \theta'^2) \sqrt{k_0^2 \theta'^2 + \kappa_F^2 \varphi'^2}}{\sinh\left(2\beta c_l \sqrt{k_0^2 \theta'^2 + \kappa_F^2 \varphi'^2}\right)}, \quad (\text{E1})$$

where B is defined in Eq. (D2) and $a_{x,y} = 1, a_z = 0$. After the change of variables (D3), the integral becomes

$$\Gamma_{\text{tr}}^i = \frac{2B}{(2\beta c_l)^5 \kappa_F^3 k_0} \int_0^{\beta c_l \kappa_F \pi} dy \int_0^{\beta c_l k_0 \pi} dx \frac{\sqrt{x^2 + y^2}}{\sinh \sqrt{x^2 + y^2}} \times \left(y^2 + a_i \left(\frac{\kappa_F}{k_0} \right)^2 x^2 \right). \quad (\text{E2})$$

Extending the integration limits to ∞ and using

$$\int_0^\infty dy \int_0^\infty dx \frac{x^2 \sqrt{x^2 + y^2}}{\sinh \sqrt{x^2 + y^2}} = \frac{93\pi\zeta(5)}{8}, \quad (\text{E3})$$

we obtain

$$\Gamma_{\text{tr}}^i = \frac{93\pi\zeta(5)B}{4(2\beta c_l)^5 \kappa_F^3 k_0} \left[1 + a_i \left(\frac{\kappa_F}{k_0} \right)^2 \right]. \quad (\text{E4})$$

Neglecting the term of order $(\kappa_F/k_0)^2$ gives Eq. (58).

2. Intermediate temperature

When $T_{\text{BG}}^{(\text{pol})} \ll T \ll T_{\text{BG}}^{(\text{tor})}$, we may still linearize $\sin \theta'$, but not $\sin \varphi'$. Using Eq. (D3) gives

$$\Gamma_{\text{tr}}^i = \frac{2B}{(2\beta c_l)^2 k_0} \int_0^{\frac{\pi}{2}} d\varphi' \int_0^{\beta c_l k_0 \pi} dx \frac{\sqrt{x^2 + b^2(\varphi')}}{\sinh \sqrt{x^2 + b^2(\varphi')}} \times \cos^2(\varphi') \left[\sin^2(\varphi') + a_i \left(\frac{x}{2\beta c_l k_0} \right)^2 \cos(2\varphi') \right], \quad (\text{E5})$$

with $b(\varphi') = 2\beta c_l \kappa_F \sin(\varphi')$. As done in Eq. (D6), we neglect $b(\varphi')$ here as well and extend the limit of x -integration, obtaining

$$\Gamma_{\text{tr}}^i = \frac{2B}{(2\beta c_l)^2 k_0} \int_0^{\frac{\pi}{2}} d\varphi' \int_0^{\infty} dx \frac{x}{\sinh x} \cos^2(\varphi') \times \left[\sin^2(\varphi') + a_i \left(\frac{x}{2\beta c_l k_0} \right)^2 \cos(2\varphi') \right]. \quad (\text{E6})$$

Performing the φ' and x integrations yields

$$\Gamma_{\text{tr}}^i = \frac{\pi^3 B}{32(2\beta c_l)^2 k_0} \left[1 + a_i \left(\frac{\pi}{2\beta c_l k_0} \right)^2 \right]. \quad (\text{E7})$$

In this regime, we see that the second term in Γ_{tr}^i is suppressed by the factor $(\beta c_l k_0)^{-2} \ll 1$ and can be safely neglected, yielding Eq. (59).

3. High temperature

When $T_{\text{BG}}^{(\text{pol})} \ll T_{\text{BG}}^{(\text{tor})} \ll T$, we linearize the denominator by using $\sinh x \approx x$ and obtain

$$\Gamma_{\text{tr}}^i = 2B \int_0^{\frac{\pi}{2}} d\varphi' \int_0^{\frac{\pi}{2}} d\theta' \frac{1}{2\beta c_l} \cos^2(\varphi') \times [\sin^2 \varphi' + a_i \cos(2\varphi') \sin^2 \theta']. \quad (\text{E8})$$

Performing the φ' and θ' integrations gives Eq. (60).

-
- [1] O. Vafeek and A. Vishwanath, Dirac Fermions in Solids: From High-Tc Cuprates and Graphene to Topological Insulators and Weyl Semimetal, *Annual Review of Condensed Matter Physics* **5**, 83 (2014).
- [2] A. A. Burkov, Topological semimetals, *Nature Materials* **15**, 1145 (2016).
- [3] N. P. Armitage, E. J. Mele, and A. Vishwanath, Weyl and Dirac semimetals in three-dimensional solids, *Rev. Mod. Phys.* **90**, 015001 (2018).
- [4] B. Q. Lv, T. Qian, and H. Ding, Experimental perspective on three-dimensional topological semimetals, *Rev. Mod. Phys.* **93**, 025002 (2021).
- [5] L. M. Schoop, F. Pielnhofer, and B. V. Lotsch, Chemical Principles of Topological Semimetals, *Chemistry of Materials* **30**, 3155 (2018).
- [6] A. A. Burkov, M. D. Hook, and L. Balents, Topological nodal semimetals, *Phys. Rev. B* **84**, 235126 (2011).
- [7] C. Fang, Y. Chen, H.-Y. Kee, and L. Fu, Topological nodal line semimetals with and without spin-orbital coupling, *Phys. Rev. B* **92**, 081201 (2015).
- [8] Y.-H. Chan, C.-K. Chiu, M. Y. Chou, and A. P. Schnyder, Ca_3P_2 and other topological semimetals with line nodes and drumhead surface states, *Phys. Rev. B* **93**, 205132 (2016).
- [9] S.-Y. Yang, H. Yang, E. Derunova, S. S. P. Parkin, B. Yan, and M. N. Ali, Symmetry demanded topological nodal-line materials, *Advances in Physics: X* **3**, 1414631 (2018).
- [10] Y. H. Kwan, P. Reiss, Y. Han, M. Bristow, D. Prabhakaran, D. Graf, A. McCollam, S. A. Parameswaran, and A. I. Coldea, Quantum oscillations probe the Fermi surface topology of the nodal-line semimetal CaAgAs , *Phys. Rev. Res.* **2**, 012055 (2020).
- [11] L. M. Schoop, M. N. Ali, C. Straßer, A. Topp, A. Varykhalov, D. Marchenko, V. Duppel, S. S. P. Parkin, B. V. Lotsch, and C. R. Ast, Dirac cone protected by non-symmorphic symmetry and three-dimensional Dirac line node in ZrSiS , *Nature Communications* **7**, 11696 (2016).
- [12] M. Neupane, I. Belopolski, M. M. Hosen, D. S. Sanchez, R. Sankar, M. Szlowska, S.-Y. Xu, K. Dimitri, N. Dhakal, P. Maldonado, P. M. Oppeneer, D. Kaczorowski, F. Chou, M. Z. Hasan, and T. Durakiewicz, Observation of topological nodal fermion semimetal phase in ZrSiS , *Phys. Rev. B* **93**, 201104 (2016).
- [13] B.-B. Fu, C.-J. Yi, T.-T. Zhang, M. Caputo, J.-Z. Ma, X. Gao, B. Q. Lv, L.-Y. Kong, Y.-B. Huang, P. Richard, M. Shi, V. N. Strocov, C. Fang, H.-M. Weng, Y.-G. Shi, T. Qian, and H. Ding, Dirac nodal surfaces and nodal lines in ZrSiS , *Science Advances* **5**, eaau6459 (2019).
- [14] X. Wang, X. Pan, M. Gao, J. Yu, J. Jiang, J. Zhang, H. Zuo, M. Zhang, Z. Wei, W. Niu, Z. Xia, X. Wan, Y. Chen, F. Song, Y. Xu, B. Wang, G. Wang, and R. Zhang, Evidence of Both Surface and Bulk Dirac Bands and Anisotropic Nonsaturating Magnetoresistance in ZrSiS , *Advanced Electronic Materials* **2**, 1600228 (2016).
- [15] M. N. Ali, L. M. Schoop, C. Garg, J. M. Lippmann, E. Lara, B. Lotsch, and S. S. P. Parkin, Butterfly magnetoresistance, quasi-2D Dirac Fermi surface and topological phase transition in ZrSiS , *Science Advances* **2**, e1601742 (2016).
- [16] R. Singha, A. K. Pariari, B. Satpati, and P. Mandal, Large nonsaturating magnetoresistance and signature of nondegenerate Dirac nodes in ZrSiS , *Proceedings of the National Academy of Sciences* **114**, 2468 (2017).
- [17] R. Sankar, G. Peramaiyan, I. P. Muthuselvam, C. J. Butler, K. Dimitri, M. Neupane, G. N. Rao, M.-T. Lin, and F. C. Chou, Crystal growth of Dirac semimetal ZrSiS with high magnetoresistance and mobility, *Scientific Re-*

- ports **7**, 40603 (2017).
- [18] M. Matusiak, J. R. Cooper, and D. Kaczorowski, Thermoelectric quantum oscillations in ZrSiS, *Nature Communications* **8**, 15219 (2017).
- [19] J. Hu, Z. Tang, J. Liu, Y. Zhu, J. Wei, and Z. Mao, Nearly massless Dirac fermions and strong Zeeman splitting in the nodal-line semimetal ZrSiS probed by de Haas–van Alphen quantum oscillations, *Phys. Rev. B* **96**, 045127 (2017).
- [20] S. Pezzini, M. R. van Delft, L. M. Schoop, B. V. Lotsch, A. Carrington, M. I. Katsnelson, N. E. Hussey, and S. Wiedmann, Unconventional mass enhancement around the Dirac nodal loop in ZrSiS, *Nature Physics* **14**, 178 (2018).
- [21] M.-X. Yang, W. Luo, and W. Chen, Quantum transport in topological nodal-line semimetals, *Advances in Physics: X* **7**, 2065216 (2022).
- [22] S. V. Syzranov and B. Skinner, Electron transport in nodal-line semimetals, *Phys. Rev. B* **96**, 161105 (2017).
- [23] J. Hu, S.-Y. Xu, N. Ni, and Z. Mao, Transport of Topological Semimetals, *Annual Review of Materials Research* **49**, 207 (2019).
- [24] W. Chen, H.-Z. Lu, and O. Zilberberg, Weak Localization and Antilocalization in Nodal-Line Semimetals: Dimensionality and Topological Effects, *Phys. Rev. Lett.* **122**, 196603 (2019).
- [25] J. Zhang, M. Gao, J. Zhang, X. Wang, X. Zhang, M. Zhang, W. Niu, R. Zhang, and Y. Xu, Transport evidence of 3D topological nodal-line semimetal phase in ZrSiS, *Frontiers of Physics* **13**, 137201 (2018).
- [26] A. V. Pronin and M. Dressel, Nodal Semimetals: A Survey on Optical Conductivity, *physica status solidi (b)* **258**, 2000027 (2021).
- [27] H. Yang, R. Moessner, and L.-K. Lim, Quantum oscillations in nodal line systems, *Phys. Rev. B* **97**, 165118 (2018).
- [28] C. Li, C. M. Wang, B. Wan, X. Wan, H.-Z. Lu, and X. C. Xie, Rules for Phase Shifts of Quantum Oscillations in Topological Nodal-Line Semimetals, *Phys. Rev. Lett.* **120**, 146602 (2018).
- [29] S. Pradhan, S. K. Pradhan, P. Mal, P. Rambabu, A. Lakhani, B. Das, B. L. Chittari, G. R. Turpu, and P. Das, Topological nodal line features in NiSe semimetal: Insights from electronic transport and density functional theory studies, *Phys. Rev. B* **110**, 195153 (2024).
- [30] P. Chakraborty, A. Hui, G. Bednik, and B. Skinner, Magnetothermopower of Nodal-Line Semimetals, *PRX Energy* **3**, 023007 (2024).
- [31] F. H. Rather, F. Haidar, M. J. A., and I. Mandal, Direction-dependent linear response for gapped nodal-line semimetals in planar-Hall configurations, *The European Physical Journal B* **99**, 41 (2026).
- [32] A. N. Rudenko and S. Yuan, Electron-phonon interaction and zero-field charge carrier transport in the nodal-line semimetal ZrSiS, *Phys. Rev. B* **101**, 115127 (2020).
- [33] B. M. Fregoso, M. Neupane, and A. P. Sakhya, Energy relaxation dynamics in a nodal-line semimetal, *Phys. Rev. B* **105**, 144304 (2022).
- [34] H.-J. Lin, T. Liu, and H.-Z. Lu, Quantum oscillations in acoustic phonons of nodal-line semimetals, *Phys. Rev. B* **109**, 195421 (2024).
- [35] Y. Suzumura, R. Kato, and M. Ogata, Electric transport of nodal line semimetals in single-component molecular conductors, *Crystals* **10**, 862 (2020).
- [36] G. Bian, T.-R. Chang, R. Sankar, S.-Y. Xu, H. Zheng, T. Neupert, C.-K. Chiu, S.-M. Huang, G. Chang, I. Belopolski, D. S. Sanchez, M. Neupane, N. Alidoust, C. Liu, B. Wang, C.-C. Lee, H.-T. Jeng, C. Zhang, Z. Yuan, S. Jia, A. Bansil, F. Chou, H. Lin, and M. Z. Hasan, Topological nodal-line fermions in spin-orbit metal PbTaSe₂, *Nature Communications* **7**, 10556 (2016).
- [37] M. M. Hosen, K. Dimitri, I. Belopolski, P. Maldonado, R. Sankar, N. Dhakal, G. Dhakal, T. Cole, P. M. Oppeneer, D. Kaczorowski, F. Chou, M. Z. Hasan, T. Durakiewicz, and M. Neupane, Tunability of the topological nodal-line semimetal phase in ZrSiX-type materials ($X = \text{S, Se, Te}$), *Phys. Rev. B* **95**, 161101 (2017).
- [38] J. M. Ziman, *Electrons and phonons*, International series of monographs on physics (Clarendon Press, Oxford, 1960).
- [39] N. Ashcroft and N. Mermin, *Solid State Physics*, HRW international editions (Holt, Rinehart and Winston, 1976).
- [40] M. S. Fuhrer, Textbook physics from a cutting-edge material, *Physics* **3**, 106 (2010).
- [41] F. Bucchieri, A. De Martino, R. G. Pereira, P. W. Brouwer, and R. Egger, Phonon-limited transport and Fermi arc lifetime in Weyl semimetals, *Phys. Rev. B* **105**, 085410 (2022).
- [42] R. G. Pereira, F. Bucchieri, A. De Martino, and R. Egger, Superconductivity from piezoelectric interactions in Weyl semimetals, *Phys. Rev. B* **100**, 035106 (2019).
- [43] S. Galeski, K. Araki, O. K. Forslund, R. Wawrzyńczak, H. F. Legg, P. K. Sivakumar, U. Miniotaite, F. Elson, M. Månsson, C. Witteveen, F. O. von Rohr, A. Q. R. Baron, D. Ishikawa, Q. Li, G. Gu, L. X. Zhao, W. L. Zhu, G. F. Chen, Y. Wang, S. S. P. Parkin, D. Grobunov, S. Zherlitsyn, B. Vlaar, D. H. Nguyen, S. Paschen, P. Narang, C. Felser, J. Wosnitza, T. Meng, Y. Sassa, S. A. Hartnoll, and J. Gooth, Quantum oscillation signatures of the Bloch-Grüneisen temperature in the Dirac semimetal ZrTe₅, *Phys. Rev. B* **110**, L121103 (2024).
- [44] A. Topp, J. M. Lippmann, A. Varykhalov, V. Duppele, B. V. Lotsch, C. R. Ast, and L. M. Schoop, Nonsymmorphic band degeneracy at the Fermi level in ZrSiTe, *New Journal of Physics* **18**, 125014 (2016).
- [45] R. Singha, S. Samanta, S. Chatterjee, A. Pariari, D. Majumdar, B. Satpati, L. Wang, A. Singha, and P. Mandal, Probing lattice dynamics and electron-phonon coupling in the topological nodal-line semimetal ZrSiS, *Phys. Rev. B* **97**, 094112 (2018).
- [46] S. Xue, T. Zhang, C. Yi, S. Zhang, X. Jia, L. H. Santos, C. Fang, Y. Shi, X. Zhu, and J. Guo, Electron-phonon coupling and Kohn anomaly due to floating two-dimensional electronic bands on the surface of ZrSiS, *Phys. Rev. B* **100**, 195409 (2019).
- [47] W. Zhao, E. Haque, L. Guo, D. Cortie, L. Chen, B. Salmankurt, X. Wang, R.-K. Zheng, N. V. Medhekar, J. Karel, and K. C. Rule, Phonon softening and electron-phonon coupling in the topological nodal-line semimetal ZrGeSe, *Phys. Rev. Mater.* **8**, 034201 (2024).
- [48] W. G. Baber, The contribution to the electrical resistance of metals from collisions between electrons, *Proceedings of the Royal Society of London. Series A, Mathematical and Physical Sciences* **158**, 383 (1937).
- [49] H. Huang, W. Jiang, K.-H. Jin, and F. Liu, Tunable topological semimetal states with ultraflat nodal rings

- in strained YN, *Phys. Rev. B* **98**, 045131 (2018).
- [50] L. Landau, E. Lifshitz, A. Kosevich, and L. Pitaevskii, *Theory of Elasticity: Volume 7*, Course of theoretical physics (Butterworth-Heinemann, 1986).
- [51] T. Matsushita, S. Fujimoto, and A. P. Schnyder, Topological piezoelectric effect and parity anomaly in nodal line semimetals, *Phys. Rev. Res.* **2**, 043311 (2020).
- [52] A. L. Kholkin, N. A. Pertsev, and A. V. Goltsev, *Piezoelectric and Acoustic Materials for Transducer Applications*, edited by A. Safari and E. K. Akdoğan (Springer US, Boston, MA, 2008) pp. 17–38.
- [53] A. Muhasin Reza and S. Naqib, DFT based investigation of bulk mechanical, thermophysical and optoelectronic properties of PbTaSe₂ topological semimetal, *Computational Condensed Matter* **36**, e00833 (2023).
- [54] C. S. A. Müller, T. Khouri, M. R. van Delft, S. Pezzini, Y.-T. Hsu, J. Ayres, M. Breitzkreiz, L. M. Schoop, A. Carrington, N. E. Hussey, and S. Wiedmann, Determination of the Fermi surface and field-induced quasiparticle tunneling around the Dirac nodal loop in ZrSiS, *Phys. Rev. Res.* **2**, 023217 (2020).
- [55] C.-L. Zhang, Z. Yuan, G. Bian, S.-Y. Xu, X. Zhang, M. Z. Hasan, and S. Jia, Superconducting properties in single crystals of the topological nodal semimetal PbTaSe₂, *Phys. Rev. B* **93**, 054520 (2016).
- [56] S. M. Girvin and K. Yang, *Modern Condensed Matter Physics* (Cambridge University Press, 2019).
- [57] G. D. Mahan, *Many-Particle Physics*, 3rd ed., Physics of Solids and Liquids (Springer US, 2000).
- [58] J. A. Sobota, Y. He, and Z.-X. Shen, Angle-resolved photoemission studies of quantum materials, *Rev. Mod. Phys.* **93**, 025006 (2021).
- [59] S. Ahn, E. J. Mele, and H. Min, Electrodynamics on Fermi Cyclides in Nodal Line Semimetals, *Phys. Rev. Lett.* **119**, 147402 (2017).
- [60] E. Emmanouilidou, B. Shen, X. Deng, T.-R. Chang, A. Shi, G. Kotliar, S.-Y. Xu, and N. Ni, Magnetotransport properties of the single-crystalline nodal-line semimetal candidates CaTX ($T = \text{Ag, Cd}$; $X = \text{As, Ge}$), *Phys. Rev. B* **95**, 245113 (2017).
- [61] A. Anand and A. De Martino, Toroidal Fermi-surface geometry and phonon-limited transport in nodal-line semimetals. Zenodo. (2025), <https://doi.org/10.5281/zenodo.18023051>.